Local circuit amplification of spatial selectivity in the hippocampus

Tristan Geiller[1,2*], Sadra Sadeh[3], Sebastian V. Rolotti[1,2], Heike Blockus[1,2], Bert Vancura[1,2], Adrian Negrean[1,2], Andrew J. Murray[4], Balázs Rózsa[5], Franck Polleux[1,2,6], Claudia Clopath[3], and Attila Losonczy[1,2,6*]

1) Department of Neuroscience, Columbia University, New York, NY, USA
2) Mortimer B. Zuckerman Mind Brain Behavior Institute, Columbia University, New York, NY, USA
3) Bioengineering Department, Imperial College London, London, UK
4) Sainsbury Wellcome Centre, University College London, London, UK
5) Institute of Experimental Medicine, Budapest, Hungary
6) The Kavli Institute for Brain Science, Columbia University, New York, NY, USA

[*]Correspondence should be addressed to T.G.: tcg2117@columbia.edu, or A.L.: al2856@columbia.edu

Abstract

Local circuit architecture facilitates the emergence of feature selectivity in the cerebral cortex[1]. In the hippocampus, it remains unknown whether local computations supported by specific connectivity motifs[2] regulate the spatial receptive fields of pyramidal cells[3]. Here, we developed an *in vivo* electroporation method for monosynaptic retrograde tracing[4] and optogenetics manipulation at single-cell resolution to interrogate the dynamic interaction of place cells with their microcircuitry during navigation. We found a previously unrecognized local circuit mechanism in CA1 whereby the spatial tuning of an individual place cell can propagate to a functionally recurrent subnetwork[5] to which it belongs. The emergence of place fields in individual neurons led to the development of inverse selectivity in a subset of their presynaptic interneurons, and recruited functionally coupled place cells at that location. Thus, the spatial selectivity of single CA1 neurons is amplified through local circuit plasticity to enable effective multi-neuronal representations that can flexibly scale environmental features locally without degrading the feedforward input structure.

Main

Hippocampal functions supporting memory and navigation[6] are traditionally investigated at the level of feature selectivity in single place cells[7] or circuit-level representations such as cognitive maps[8], leaving a major disconnect between these levels of implementation. Mesoscale circuit motifs emerging from small numbers of functionally arranged excitatory principal cells and inhibitory interneurons are posited to bridge the gap between single-cell operations and macroscopic cognitive functions[9,10]. Indeed, manipulation of individual cells has been shown to elicit detectable effects on circuit dynamics and ultimately behavior[11], exemplifying the importance of understanding how single neurons are embedded within multi-cellular ensembles to perform specific functions[12]. In the hippocampus, the functional organization of identified local circuits has been largely unexplored. In the traditional view of hippocampal area CA1, spatial tuning emerges in a subset of pyramidal cells (PCs) based on their feedforward inputs[13], and thus, it remains unknown whether CA1 can also flexibly regulate spatial selectivity through local computations. This major knowledge gap stems from notorious difficulties in accessing synaptically coupled microcircuits *in vivo*, and in unambiguously restricting optogenetic manipulations to individual neurons, particularly within the dense structure of the pyramidal cell layer. Here we leveraged single-cell labeling, tracing, and optogenetics manipulations to uncover the mesoscale determinants of CA1 circuit functions.

Single-cell retrograde tracing in CA1

We first adapted a single-cell electroporation approach[4,9] and applied it to the mouse dorsal hippocampus in order to genetically label neurons *in vivo* and perform monosynaptic rabies (RABV) tracing[14] from single CA1 starter PCs (**Fig 1a**). An individual neuron was electroporated with three plasmids: the RABV-TVA receptor, the glycoprotein (G), and a fluorescent protein (Venus) (**Fig. 1b**). After 2 days post-electroporation, an envelope-A (EnvA) coated, G-deleted N2C tdTomato-RABV[14] was injected in the vicinity of the starter cell (**Fig. 1c**). After 10-14 days, tdTomato-expressing presynaptic neurons could be seen throughout the hippocampus (**Fig. 1c, 1d, 1e, ED1, Supplementary Table 1**). Our quantification of the connectivity within CA1 revealed that 90.7±0.02% (mean±sd) of the local inputs to a starter PC were inhibitory interneurons (**ED1**).

We next sought to interrogate the functional coupling of individual place cells with their local presynaptic partners using this method. Given the larger number of local inhibitory connections, we examined whether spatial tuning in a starter PC could vary with the level of inhibition provided by its presynaptic interneurons (**Fig. 1f**). To do so, we expressed a genetically-encoded Ca^{2+} indicator (GcaMP7) in all inhibitory interneurons using the VGAT-Cre driver line (**Fig. 1g**). In the same mouse, we electroporated a starter PC with to express the receptor TVA, the RABV-G, GCaMP and mRuby3 acting as a static marker (**Fig. 1h**). The mice were trained to run on a linear treadmill enriched with sensory cues[15], and we then performed two-photon (2p) imaging of the starter cell and local interneurons using large-scale volumetric methods[16] (**Fig. 1i)**. Injection of the tdTomato-RABV was subsequent to 2p imaging to prevent potential toxicity confounds inherent to RABV (**Fig. 1i**). Thus, the identity of each interneuron (tdTomato-expressing **presynaptic** vs. non-expressing **unlabeled**) was mapped retrospectively to its *in vivo* dynamics 14-21 days after RABV injection (**Fig. 1j**). In total, we recorded 19 starter pyramidal cells together with their respective presynaptic interneurons, which we will refer to as “network”. (**Supplementary Table 2**).

80 **Inhibition during place field formation**
81 We first parceled each imaging session based on the spatial response of the starter PC. In 11 of the
82 19 networks, we recorded the spontaneous formation of a place field, defined by the sudden
83 appearance of a large-amplitude Ca^{2+} transient and smaller repeated events in the following
84 traversals[17] (**ED 2a**). The appearance of this first event did not coincide with a change in the activity
85 levels of the presynaptic interneurons, as neither a global decrease in activity was observed
86 preceding the lap of formation (**ED 2b, 2c**), nor a local reconfiguration of their spatial response was
87 observed at that location (**ED 2d, 2e**). To quantify the response on a cell-by-cell basis, we calculated
88 the in-field selectivity (IFS) index, a measure for whether a given interneuron is more (IFS closer to 1)
89 or less (IFS closer to -1) active within the starter's place field than outside. Using this index, we
90 assessed the change in activity around the place field location but did not detect significant changes
91 during the formation lap, in the laps preceding the formation, or following it (**ED 2f, 2g**). These results
92 show that presynaptic inhibition stayed relatively constant during, and immediately following the
93 formation of a place field in their target PC, arguing for a lack of major contribution from interneurons
94 in this process.
95
96 **Presynaptic inhibition is inversely tuned**
97 We next examined whether the spatial activity of interneurons was different when the starter PC had
98 an already established place field. In 8 of the 19 networks, the activity of the starter cell was selective
99 to a specific location on the belt (place cell) from the first lap of the session (**Fig. 2a, 2b**). The activity
100 of the interneurons was high across the belt[16] (**Fig. 2a, 2b**), but we observed that presynaptic
101 interneurons had lower activity than the unlabeled ones during the traversal of the place field (**Fig. 2a,**
102 **2b**). The difference in activity between the two populations was indeed significantly different only in
103 close vicinity of the place field peak (**Fig. 2c, 2d**). To examine this effect on a cell-by-cell basis, we
104 used the IFS index to quantify the degree of selectivity in each population. We found that presynaptic
105 interneurons had significantly more negative IFS values (**Fig. 2e**), indicating that the overall decrease
106 seen at the population level was not driven by a small number of interneurons with large negative
107 responses. We computed an average IFS value for each network and observed the same effect (**Fig.**
108 **2f, data**). By contrast, the two populations were not significantly different when the IFS index was
109 computed at a random location on the belt, irrespective of the location of the place field (**Fig. 2f,**
110 **shuffle**), or when the starter cell was not spatially tuned (**ED3a-d**). These results demonstrate that
111 presynaptic inhibition is lower during the traversal of a stable, but not a newly formed spatial receptive
112 field. In 4 of the 8 networks analyzed above, we recorded the formation of the field in a directly
113 preceding session (**ED3e, 3f**), and found that the rest period between the two sessions induced a
114 substantial reconfiguration that led to the negative tuning in the presynaptic interneurons (**ED3g-j**).
115 Together, these results demonstrate that emergence of a spatial receptive field in place cells triggers
116 plastic reorganization in CA1 local circuits that ultimately leads to negative selectivity in their own
117 presynaptic inhibitory ensemble.
118
119 **Reorganization of interneuron dynamics**
120 Thus far, we found that local circuit plasticity can promote correlative dynamics between single-cell
121 representations and interneuron selectivity during navigation. It remains unknown, however, whether
122 place cells can individually generate such location-specific reconfigurations. To causally test this
123 hypothesis, we developed an optogenetic approach to induce individual place fields at predetermined

locations[17], while longitudinally tracking the reorganization this generates from an experimenter-defined time-zero (**Supplementary Table 3**). We electroporated a single PC, referred to as seed neuron, with a red-shifted excitatory opsin (**Fig. 3a**) that we photostimulated[18] at an arbitrary location (in a PRE session) to generate a place field that could last in post-stimulation laps after rest (POST) in the home cage (7 successful sessions out of 14, n = 6 mice) (**Fig. 3b)**. We used this procedure in VGAT-Cre mice to monitor how the controlled implantation of a place cell reconfigured interneuronal dynamics at this location (**Fig. 3c**). Consistent with previous reports[19], the seed stimulations increased the activity of interneurons above baseline (**Fig. 3d, ED4a, 4b)**, and without noticeable changes in behavior (**ED4c, 4d**). When induction was successful (+), a subset of interneurons reconfigured their spatial response to develop inverse tuning around that location in POST (**Fig. 3e, 3f**). We quantified the degree of inverse selectivity on a cell-by-cell basis (**Fig. 3g**), and observed that the increase in activity in the induction laps in PRE correlated with how strongly anti-selective an interneuron would become in the POST session (**Fig. 3h, ED4c, 4d**). This reorganization pattern was not present when induction failed (-) or during laps immediately following photostimulation (**ED5a-d**), consistent with the development of inverse selectivity not directly following endogenous place field formation in our first set of experiments. Similarly, the induced location was not already biased with a higher fraction of negatively selective interneurons prior to induction (**ED5e-g**). Together these results further demonstrate that place field formation in an individual CA1 PC can robustly promote plastic reorganization in local circuits.

Pyramidal cells are functionally coupled

To further understand the extent to which a single PC can influence the local circuitry, we next examined the effects exerted on the local pyramidal population. We induced seed neurons as described above (**Fig. 3b**) while performing large scale population imaging (**Fig. 4a**). We observed that photostimulation of the seed neuron elevated the number of Ca^{2+} events in other local PCs[20] (**Fig. 4b**, **ED6a, 6b**), which was not seen before any seed was electroporated in the brain, and indicating that photostimulations alone cannot explain this effect (**Fig. 4c**). We found that the PCs which displayed an elevated response to photostimulations, referred to as recruited neurons (across sessions mean±sem: 12.6±1.6 neurons, **ED6c-f**), were significantly more likely to be spatially tuned in the POST session (**Fig. 4e**). Importantly, this quantification was restricted to the recruited neurons that were not already tuned in PRE, and this effect was seen only when induction was successful (**Fig. 4e)**. Additionally, the distribution of fields for these new place cells in POST had a higher density around the location where the seed PC was induced in PRE (**Fig. 4f, 4g, ED7**). Together these results demonstrate that the successful formation of a place field in an individual seed neuron can recruit a subset of PCs which will become spatially tuned at that location. Finally, we detected traces of this ensemble organization during periods of immobility and navigation prior to induction of the seed neuron, demonstrating the presence of already coupled PCs with distance-dependent like-to-like relationships (**ED6g-k, ED4g-j**). With such configuration, CA1 circuits can thus propagate spatial representations originating in an individual neuron to a multi-cellular assembly, without biasing the global representation of the context at the population level (**ED7**).

Subnetwork structure of the CA1 circuit

Finally, in order to explore what structure and plasticity rules are necessary to support our experimental data, we developed a computational model of hippocampal region CA1

168 (**Supplementary Table 4**). First, we found that the dynamics we observed could not emerge out of
169 single-cell interactions, such that a single seed PC alone does not provide a strong enough input to
170 induce interneuron reorganization (**ED8a-d**). We then introduced some degree of connection
171 specificity through a subnetwork architecture, where the seed neuron was part of an ensemble of
172 other PCs and interneurons connected above chance level (**Fig. 4h**). The emergence of a place field
173 in a seed PC elevated the response of its postsynaptic pyramidal partners mainly within the
174 subnetwork (**Fig. 4i, 4j pre**-field formation vs. **during**-field formation). When we introduced short-term
175 synaptic depression at pyramidal-to-interneuron synapses[19], this sequence of events deprived
176 interneurons specifically within the subnetwork of their specific excitatory input at the target location
177 (**Fig. 4j, post**-field formation) and thus developed a selective decrease in their activity where the field
178 was initially formed. And finally, the decreased level of inhibition in turn facilitates the amplification of
179 this location by other PCs of the subnetwork (**ED9a**). This model is consistent with subnetwork of
180 different sizes (**ED8e-h**), but the reciprocal coupling between PCs and interneurons within the
181 subnetwork as well as specific PC interconnectivity are necessary to recapitulate our observations
182 (**ED9b-e**). An alternative model based on direct disinhibitory circuitry could not recapitulate our
183 findings (**ED10**).
184

185 **Discussion**

186 Our results provide important insights into the microcircuit mechanisms underlying feature selectivity
187 in CA1, consistent with a lack of a permissive role for disinhibition in place field formation[21] but
188 arguing against spatially uniform inhibition during place field maintenance. Moreover, CA1 PCs do not
189 operate as independent coding units. Rather, coordinated connectivity and plasticity between co-
190 active PCs and associated inhibitory subnetworks enable feature selective responses initiated in
191 single cells to scale adaptively to multi-cellular assemblies. This local amplification could enable
192 flexible and efficient encoding of behaviorally relevant environmental features locally within the CA1
193 region. Finally, our results suggest that CA1 PCs are more functionally coupled than previously
194 considered. The nature of these connections may be monosynaptic[20] polysynaptic with non-random
195 motifs[22] or through jap junctions[23]. Relatedly, short-term synaptic plasticity of excitatory input and
196 inhibitory output synapses of interneurons[24] could also contribute to the local circuit reorganization we
197 describe. We speculate that such subnetwork structure may be optimized for providing CA1 the ability
198 to assign behavioral salience to CA3 representations through local circuit amplification, without
199 compromising overall storage capacity or specificity.
200 The precise anatomical organization and fine-scale subnetwork connectivity underlying the initial
201 motif structure and governing its propagation are currently unknown. They can arise during
202 development[25,26] or from experience-dependent structural plasticity[27]. Furthermore, the gradual
203 expression of local circuit reorganization suggests that an initial, rapid place field formation event[17] in
204 an individual or a few seed neurons can subsequently propagate through their associated subnetwork
205 via slower and more graded plasticity mechanisms. The precise loci and molecular mechanisms of
206 neural plasticity[28,29] underlying this local circuit amplification of feature selectivity remain to be
207 determined.
208

209
210 **References:**
211
212 1. Miller, K. D. Canonical computations of cerebral cortex. *Current Opinion in Neurobiology* vol. 37 75–84
213 (2016).
214 2. Jiang, X. *et al.* Principles of connectivity among morphologically defined cell types in adult neocortex.
215 *Science* **350**, (2015).
216 3. O'Keefe, J. & Dostrovsky, J. The hippocampus as a spatial map. Preliminary evidence from unit activity
217 in the freely-moving rat. *Brain Research* **34**, 171–175 (1971).
218 4. Wertz, A. *et al.* Single-cell-initiated monosynaptic tracing reveals layer-specific cortical network modules.
219 *Science* (2015) doi:10.1126/science.aab1687.
220 5. Najafi, F. *et al.* Excitatory and Inhibitory Subnetworks Are Equally Selective during Decision-Making and
221 Emerge Simultaneously during Learning. *Neuron* **105**, 165–179 (2020).
222 6. Eichenbaum, H. A cortical–hippocampal system for declarative memory. *Nature Reviews Neuroscience*
223 **1**, 41–50 (2000).
224 7. Epsztein, J., Brecht, M. & Lee, A. K. Intracellular Determinants of Hippocampal CA1 Place and Silent
225 Cell Activity in a Novel Environment. *Neuron* **70**, 109–120 (2011).
226 8. Stachenfeld, K. L., Botvinick, M. M. & Gershman, S. J. The hippocampus as a predictive map. *Nature*
227 *Neuroscience* **20**, 1643–1653 (2017).
228 9. Rossi, L. F., Harris, K. D. & Carandini, M. Spatial connectivity matches direction selectivity in visual
229 cortex. *Nature* **588**, 648–652 (2020).
230 10. Sadeh, S. & Clopath, C. Inhibitory stabilization and cortical computation. *Nature Reviews Neuroscience*
231 vol. 22 21–37 (2021).
232 11. Houweling, A. R. & Brecht, M. Behavioural report of single neuron stimulation in somatosensory cortex.
233 *Nature* **451**, 65–68 (2008).
234 12. Cossell, L. *et al.* Functional organization of excitatory synaptic strength in primary visual cortex. *Nature*
235 **518**, 399–403 (2015).
236 13. Kesner, R. P. & Rolls, E. T. A computational theory of hippocampal function, and tests of the theory:
237 New developments. *Neuroscience and Biobehavioral Reviews* vol. 48 92–147 (2015).
238 14. Reardon, T. R. *et al.* Rabies Virus CVS-N2cδG Strain Enhances Retrograde Synaptic Transfer and
239 Neuronal Viability. *Neuron* (2016) doi:10.1016/j.neuron.2016.01.004.
240 15. Geiller, T., Fattahi, M., Choi, J. S. & Royer, S. Place cells are more strongly tied to landmarks in deep
241 than in superficial CA1. *Nature Communications* **8**, 1–11 (2017).
242 16. Geiller, T. *et al.* Large-Scale 3D Two-Photon Imaging of Molecularly Identified CA1 Interneuron
243 Dynamics in Behaving Mice. *Neuron* **108**, 968-983.e9 (2020).
244 17. Bittner, K. C. *et al.* Conjunctive input processing drives feature selectivity in hippocampal CA1 neurons.
245 *Nature Neuroscience* (2015) doi:10.1038/nn.4062.
246 18. Kaufman, A. M., Geiller, T. & Losonczy, A. A Role for the Locus Coeruleus in Hippocampal CA1 Place
247 Cell Reorganization during Spatial Reward Learning. *Neuron* **105**, 1018-1026.e4 (2020).
248 19. English, D. F. *et al.* Pyramidal Cell-Interneuron Circuit Architecture and Dynamics in Hippocampal
249 Networks. *Neuron* **96**, 505-520.e7 (2017).
250 20. Yang, S. *et al.* Interlamellar CA1 network in the hippocampus. *Proceedings of the National Academy of*
251 *Sciences of the United States of America* **111**, 12919–12924 (2014).
252 21. Grienberger, C., Milstein, A. D., Bittner, K. C., Romani, S. & Magee, J. C. Inhibitory suppression of
253 heterogeneously tuned excitation enhances spatial coding in CA1 place cells. *Nature Neuroscience* **20**,
254 417–426 (2017).
255 22. Guzman, S. J., Schlögl, A., Frotscher, M. & Jonas, P. Synaptic mechanisms of pattern completion in the
256 hippocampal CA3 network. *Science* **353**, 1117–1123 (2016).

257 23. Draguhn, A., Traub, R. D., Schmitz, D. & Jefferys, J. G. R. Electrical coupling underlies high-frequency
258 oscillations in the hippocampus in vitro. *Nature 1998 394:6689* **394**, 189–192 (1998).
259 24. Hefft, S. & Jonas, P. Asynchronous GABA release generates long-lasting inhibition at a hippocampal
260 interneuron-principal neuron synapse. *Nature Neuroscience* **8**, 1319–1328 (2005).
261 25. Xu, H. T. *et al.* Distinct lineage-dependent structural and functional organization of the hippocampus.
262 *Cell* **157**, 1552–1564 (2014).
263 26. Picardo, M. A. *et al.* Pioneer GABA cells comprise a subpopulation of hub neurons in the developing
264 hippocampus. *Neuron* **71**, 695–709 (2011).
265 27. Caroni, P., Donato, F. & Muller, D. Structural plasticity upon learning: Regulation and functions. *Nature*
266 *Reviews Neuroscience* vol. 13 478–490 (2012).
267 28. Magee, J. C. & Grienberger, C. Synaptic Plasticity Forms and Functions. *Annual Review of*
268 *Neuroscience* vol. 43 95–117 (2020).
269 29. Mehta, M. R. From synaptic plasticity to spatial maps and sequence learning. *Hippocampus* vol. 25
270 756–762 (2015).
271 30. Kaifosh, P., Zaremba, J. D., Danielson, N. B. & Losonczy, A. SIMA: Python software for analysis of
272 dynamic fluorescence imaging data. *Frontiers in Neuroinformatics* **8**, 80 (2014).
273 31. Keemink, S. W. *et al.* FISSA: A neuropil decontamination toolbox for calcium imaging signals. *Scientific*
274 *Reports* **8**, 1–12 (2018).
275 32. Bezaire, M. J. & Soltesz, I. Quantitative assessment of CA1 local circuits: Knowledge base for
276 interneuron-pyramidal cell connectivity. *Hippocampus* **23**, 751–785 (2013).
277
278

Legends

Figure 1. In vivo single-cell electroporation and monosynaptic rabies tracing in hippocampal region CA1.

a, Schematic of *in vivo* electroporation in a CA1 starter PC. **b,** Time lapse of electroporation (top) and expression (bottom). **c,** Schematic of retrograde tracing. **d,** Light-sheet image showing presynaptic neurons (red) and the starter neuron in CA1 (green). **e,** Distribution (mean±s.e.m.) of presynaptic neurons (n=6 mice) in the hippocampus. Two-way ANOVA (region x hemisphere), interaction, P=0.079. Post hoc Tukey's tests: CA1xCA2, P=0.037; CA1xCA3, P=0.001; CA2xCA3, $P<10^{-10}$; Ipsi x Contra, $P<10^{-10}$ (adjusted for multiple comparisons). **f,** Experimental timeline for imaging and labeling interneurons presynaptic to a starter PC. **g,** Expression of the calcium indicator GCaMP is restricted to inhibitory interneurons using a VGAT-Cre driver line. **h,** One starter PC is electroporated with GCaMP and genes for the modified RABV. **i,** Z-stack projection following 2p imaging, before (left) and after (right) RABV injection. **j,** During imaging, mice run on a treadmill for randomly delivered water rewards. The identity of each recorded interneuron is assessed based on the rabies tdTomato-expression 14-21 days after data collection. All scale bars: 50µm.

Figure 2. Interneurons presynaptic to a place cell display inverse spatial selectivity.

a, Representative fluorescence traces of the starter PC and its presynaptic interneurons during navigation. **b,** Activity heatmaps along the belt (X-axis) as a function of laps (Y-axis). **c,** Spatial tuning curves (mean±s.e.m) centered around the peak of the starter's place field (n = 8 mice). Blue area with dashed lines represents the average place field size: 33.2±3.8cm (mean±s.e.m)**. d,** Difference in activity (mean±s.e.m) between the presynaptic and unlabeled interneurons from **b**, and P-value as a function of position (purple). Shaded purple area indicates when P-value<0.05 (paired t-test). **e,** In-field selectivity (IFS) index for all presynaptic (orange, n=152) and unlabeled (gray, n=1235) neurons (Kolmogorov-Smirnov two-sample test, P=0.005). Negative IFS indicates negative selectivity in the starter's place field. Inset: mean±s.e.m (t-test, P=0.002). **f,** IFS values (mean±s.e.m) for all 8 networks (data, paired t-test, P=0.001) and after shuffling the position (shuffled, paired t-test, P=0.08) of the starter's place field to recompute random IFS values (data versus shuffled for presynaptic, P=0.023; unlabeled, P=0.56, paired t-tests).

Figure 3. Optogenetic place field induction in single pyramidal cells reorganizes interneuron networks.

a, A single PC (seed) is electroporated with a red-shifted excitatory opsin and GCaMP. Optogenetics stimulations (LED) evoke large-amplitude responses. Scale bars: 15µm. **b,** Repeated optogenetics stimulations can induce a lasting place field ((+) in magenta). Failed induction sessions ((-) in gray) are used as controls in the following analyses. Place fields were induced in a PRE session and recorded again in a POST session. **c,** Z-stack projection showing GCaMP7f-expressing interneurons (green) and the seed neuron (red). Scale bar: 50µm. **d,** Photostimulation of the seed neuron during place field induction increases interneuron activity. **e,** Spatial tuning curve for all interneurons before (PRE) and after (POST) induction. Interneurons are ordered by their IFS, and centered around the induced location. A fraction of interneurons develops negative selectivity after successful inductions. **f,** Average IFS values (n=7 for each condition from 6 mice). PRE vs POST for (-), P=0.86; (+), P=0.04 (Wilcoxon rank-sum tests). **g,** IFS values for all interneurons (n=6 mice) show the development of negative selectivity after successful induction: (+), n=1208, $P<10^{-10}$; (-), n=1191, P=0.24 (Wilcoxon signed rank-tests). (+) vs (-), $P<10^{-5}$ (Wilcoxon rank-sum test). **h:** On a cell-by-cell basis, the increased activity during induction laps in PRE correlates with negative selectivity in POST: (+), n=792, P=0.004; (-), n=496, P=0.86 (Pearson's R). All boxplots represent median (central line) and interquartile range (25th and 75th percentile) while whiskers extend to the most extreme data points (excluding outliers).

329
330
331 **Figure 4. Recruitment of local pyramidal cells during place field induction is consistent with a**
332 **subnetwork architecture.**
333 **a,** Representative field of view with all CA1 PCs expressing GCaMP and one seed (red)
334 electroporated with bReaChes-mRuby3. Scale bar: 50µm. **b,** Photostimulations (arrows) drive the
335 seed neuron and evoke somatic activity in other PCs. All following data were collected from 31
336 induction sessions (13 successful and 18 failures, n=13 mice) **c,** Histogram of calcium transient
337 onsets centered around optogenetic stimulations in time. *Top:* distribution for all seed neurons.
338 *Bottom:* distribution for other PCs in the presence (blue) or absence (black) of an electroporated seed
339 neuron (Shaded area indicates bins where $P<0.05$, Fisher Z-test of proportions). **d,** Intersomatic
340 distance to the seed neuron for PCs recruited by photostimulations (n=405). **e,** Fraction of new
341 spatially selective PCs in POST. Shuffled ID indicates a randomly chosen subset of neurons
342 matching the number of recruited cells in a given session. POST(+), P=0.003; POST(-), P=0.4 (One-
343 way ANOVAs, with post-hoc Tukey's tests and P-values adjusted for multiple comparisons: recruited
344 vs nonrecruited: P=0.0093, recruited vs shuffled: P=0.0058). Recruited (POST(+) vs POST(-)),
345 P=0.006 (Wilcoxon rank-sum test). **f,** Place fields of recruited PCs are more concentrated around the
346 induced location in POST (+). **g,** Distribution of place field centroids from **f**. POST(+) vs POST(-),
347 P=0.006 (Kolmogorov-Smirnov two-sample test). Uniformity test for POST(+), n=39, P=0.019, and
348 POST(-), n=40, P=0.30. **h,** Experimental findings can be explained by a computational model with
349 subnetwork architecture. **i,** Model of de novo place field formation in a seed neuron with
350 representative tuning curves at three different time points. Average activity from 40 simulated seeds.
351 **j,** *Left:* Emergence of a field has virtually no effect on neurons outside the subnetwork of the seeds.
352 *Right:* Within the subnetwork, the location is amplified by other PCs and interneurons become
353 negatively selective. All boxplots represent median (central line) and interquartile range (25th and 75th
354 percentile) while whiskers extend to the most extreme data points (excluding outliers).
355

Materials and Methods

Experimental Model and subject details

All experiments were conducted in accordance with NIH guidelines and with the approval of the Columbia University Institutional Animal Care and Use Committee. Experiments were performed with healthy, 3-month-old heterozygous adult male and female *VGAT-ires-Cre* (Jackson Laboratory, Stock No: 016962), *VIP-ires-Cre* (Jackson Laboratory, Stock No: 031628), *R26R-EYFP* (Jackson Laboratory, Stock No: 006148) crossed with *VGAT-ires-Cre*, or wild-type (Jackson Laboratory, Stock No: 000664) mice on a C57BL/6J background. Mice were kept in the vivarium on a reversed 12-hour light/dark cycle and housed 3-5 mice in each cage (temperature: 22-23 ºC, humidity: 40%).

Viruses:

Cre-dependent recombinant adeno-associated virus (rAAV) expressing GCaMP7f under the control of the Synapsin promoter (rAAV1-Syn-FLEX-GCaMP7f-WPRE-Sv40, Addgene #104492, titer: 1×10^{13} vg/mL) was used to express GCaMP7f in VGAT-expressing interneurons or VIP-expressing interneurons. For pyramidal cell imaging, we used a forward GCaMP6f-expressing adeno-associated virus (Addgene #100833, titer: 1×10^{13} vg/mL).

Rabies virus production:

EnvA-pseudotyped CVS-N2c rabies virus was produced essentially as described previously[14]. Briefly, rabies virus was rescued via transfection of CVS-N2cΔG-tdTomato genomic plasmid, with mammalian expression plasmids for rabies virus genes P, L and M along with T7 RNA polymerase in Neuro2A cells. 6 days post-transfection supernatant containing G-coated viral particles was harvested and further amplified on Neuro2a cells stability expressing rabies G. After a further 7 days the supernatant was harvested, filtered, and applied to Neuro2A cells stably expressing the EnvA glycoprotein. After washing to remove G-coated rabies virus, EnvA-coated virus was harvested after 7 days, filtered, and concentrated by centrifugation. Viral titer was measured on HEK293 cells expressed the TVA receptor.

AAV injections and hippocampal window/headpost implant:

For viral injections, 3-5 month old mice were anesthetized with isoflurane and placed into a stereotaxic apparatus. Meloxicam and bupivacaine were administered subcutaneously to minimize discomfort. After the skin was cut in the midline to expose the skull, the skull was leveled and a craniotomy was made over the right hippocampus using a drill. A sterile glass capillary loaded with rAAV was attached to a Nanoject syringe (Drummond Scientific) and slowly lowered into the right hippocampus. Dorsal CA1 was targeted at coordinates AP -2.2, ML -1.75, DV -1.8, -1.6, -1.4, -1.2, -1 for interneuron imaging, and DV -1.2 and -1.0mm for pyramidal cell imaging, relative to Bregma, with 25 nL of virus injected at each DV location. After injection, the pipette was left in place for 5-10 minutes and slowly retracted from the brain. The skin was closed with several sutures and the mice were allowed to recover for 4 days before the window/headpost implant.

For CA1 window/headpost implant, the injected mice were anesthetized with isoflurane and placed into the stereotaxic apparatus. After subcutaneous administration of meloxicam and bupivacaine, the skull was exposed, leveled, and a 3 mm craniotomy was made over the right hippocampus, centered on coordinates AP -2.2, ML -1.75 relative to Bregma. The dura overlying the cortex was removed,

400 and the cortex overlying the hippocampus was slowly removed with negative pressure while the ice-
401 cold cortex buffer was simultaneously applied. This process was performed until the white, horizontal
402 fibers overlying CA1 became visible and any bleeding subsided. A stainless-steel cannula fitted with a
403 glass window was inserted into the craniotomy and secured in place with Vetbond applied on the
404 skull. Subsequently, dental cement was applied to the entire skull, and a headpost was affixed to the
405 posterior skull with dental cement. The mice received a 1.0 mL subcutaneous injection of PBS and
406 recovered in their home cage while heat was applied. The mice were monitored for 3 days post-
407 operatively until behavioral training began.
408
409 **Plasmid DNA:**
410 pCAG-TVA800-WT-HA was assembled via in-fusion cloning using Addgene plasmid #15778 (gift
411 from Edward Callaway). Notably, the HA-coding sequence was included in the primer sequences to
412 allow for seamless HA insertion during fusion of the TVA-PCR product into the linearized XhoI/NotI
413 pCAG vector backbone. pCAGGS-N2c(G) was a gift from Thomas Jessel, Addgene plasmid #73481.
414 pCAG-GCaMP7s was assembled via in-fusion cloning using Addgene plasmid #104487 (gift from
415 Douglas Kim) for PCR amplification as a template and inserted into NotI/XhoI sites of a pCAG-vector
416 backbone according to the manufacturer's instructions. pCAG-bReaChES-mRuby3 and pCAG-
417 ChRmine-mScarlet were constructed via infusion cloning using pAAV-CaMKIIa-bReaChes-TS-
418 mRuby3 and pAAV-CaMKIIa-ChRmine-TS-mScarlet as a PCR template (gifts from Karl Deisseroth)
419 into XhoI/NotI sites of a pCAG-vector backbone. pCAG-Cre-mRuby fusion was constructed in a two-
420 step infusion cloning process using pCAG-Cre (Addgene plasmid #13775, gift from Connie Cepko)
421 and pCAG-mRuby3 (Addgene plasmid #107744, gift from Rylan Larsen) as PCR templates to result
422 in a Cre-mRuby fusion single ORF. The PCR products were inserted in frame XhoI/NotI restriction
423 sites of a pCAG vector backbone
424
425 **Single-cell electroporation:**
426 Two-photon guided electroporation was adapted from previously described protocols[4]. 5-10 MΩ
427 borosilicate glass pipettes were pulled (DMZ Zeitz-Puller) and filled with an intracellular solution (155
428 mM K-Gluconate, 10 mM HEPES, 10 mM KCl, 40mM KOH, with 7.3 pH, 316 mOsm), Alexa Fluor 488
429 hydrazide (100μM) and a cocktail of plasmid DNA. Plasmid concentration ranged between 50 to 150
430 ng/μL, without exceeding a total concentration of 300 ng/μL. Pipettes were positioned using a
431 micromanipulator (Scientifica). Before entering the brain, a positive pressure (~30mBar) was applied.
432 Pipettes were lowered in the brain until the resistance increased by 20%. At this point, electroporation
433 was performed by applying electrical pulses. The pulses for the electroporation were powered using a
434 stimulator (ISO-Flex), generated by a digitizer (Axon Digidata 1550B) and gated with a custom-made
435 electronic circuit. Individual neurons were electroporated with a single pulse train at -5V, 100 Hz, 0.5
436 ms pulse width, 1 s duration. The success of the electroporation assessed by the spread of dye into
437 the cell, and by subsequent removal of the pipette from the area without pulling the electroporated
438 cell away. Protein expression was confirmed no less than 48 hours after electroporation. Given the
439 geometry of the brain and the design of our cannula, all electroporated neurons in CA1 resided in the
440 intermediate portion of the proximo-distal axis. Similarly, all electroporated neurons were located in
441 the deep portion of the pyramidal cell layer (closer to *stratum oriens*) for technical reasons such as
442 limiting the chance of clogging the pipette tip and preventing inadvertent electroporation of adjacent
443 neurons.

444
445 **Rabies virus injection:**
446 After imaging data was collected, 0.25 - 0.5μL of EnvA-N2cdG-tdTomato rabies virus (with a titer of
447 $1x10^8$ infectious units per ml) was loaded in a ~3 MΩ pipette and injected near the site of
448 electroporation. Expression of tdTomato became visible no less than 5 days after electroporation and
449 was monitored daily for up to 21 days post injection.
450
451 **Perfusion and tissue processing:**
452 After the completion of imaging experiments, mice were transcardially perfused with 40 mL of
453 phosphate-buffered saline (PBS, Thermo Fisher), followed by 40 mL of 4% paraformaldehyde (PFA,
454 Electron Microscopy Sciences). Brains were stored overnight in 4% PFA at 4°C. The next day, the
455 4% PFA was removed and the brains were rinsed 3x5 min in PBS. 75 um horizontal sections of the
456 imaged hippocampus were cut on a vibrating microtome (Leica VT1200S) and washed 3x15 minutes
457 in PBS. Subsequently, sections were permeabilized for 2x20 minutes in PBS with 0.3% Triton X-100
458 (Sigma-Aldrich). Blocking was then performed with 10% normal donkey serum (Jackson
459 ImmunoResearch, Catalog #017-000-121) in PBST (PBS with 0.3% Triton X-100) for 45 minutes. The
460 sections were then incubated in a PBS solution containing primary antibodies (see below for antibody
461 information and dilutions) for one hour at room temperature, followed by 2 days at 4°C. After 2 days,
462 the primary antibody solution was removed from the slices and the slices were washed 3x15 minutes
463 in PBS to remove unbound primary antibodies. The slices were subsequently incubated in a PBS
464 solution containing a mixture of appropriate secondary antibodies conjugated to fluorescent labels
465 (see below for antibody information and dilutions) for 2 hours at room temperature. The sections were
466 then washed 5x15 minutes in PBS at room temperature. Finally, sections were mounted on glass
467 slides in Fluoromount-G aqueous mounting medium (ThermoFisher Scientific) and coverslipped. The
468 slides were allowed to dry at 4°C for at least 1 day before imaging using a confocal microscope
469 (Nikon A1R). Confocal micrographs were analyzed using ImageJ 2.0.0 (NIH).
470 Whole brain clearing was performed with the iDISCO+ protocol. Mice were perfused as described
471 above and the brains were fixed overnight in 4% PFA. The brains were then slowly dehydrated in a
472 methanol/water series, incubated in a DCM/methanol mixture, bleached in 5% hydrogen peroxide in
473 methanol, and slowly rehydrated in a methanol/water series. The brains were then washed in a Triton
474 X solution, incubated in a permeabilization solution for two days and then in a blocking solution for
475 two days. The samples were subsequently incubated in primary antibody solution for 7 days, washed,
476 incubated in secondary antibody solution for 7 days, and washed again. Finally, brains were
477 dehydrated in a methanol/water series, incubated first in a DCM/methanol mixture and then in 100%
478 DCM, and stored in dibenzyl ether until imaging. Imaging was performed with a light sheet
479 microscope (Ultramicroscope II, Miltenyi Biotec) and analyzed using Imaris 9.5 (Bitplane).
480
481 **Immunohistochemistry**
482 Signals from red fluorescent proteins were amplified using the primary antibody Guinea Pig anti-RFP
483 diluted 1:500 (Synaptic Systems, #390 005) and the conjugated secondary antibody Donkey anti-
484 Guinea Pig Rhodamine Red undiluted (Jackson, 706-295-148, Lot #137877). Signals from green
485 fluorescent proteins were amplified using the primary antibody Chicken anti-GFP diluted 1:500
486 (AbCam, ab13970, Lot #GR236651-17) and the conjugated secondary antibody Donkey anti-chicken
487 Alexa 488 undiluted (Jackson, 703-545-155, Lot #138498).

Two-photon imaging:

Imaging was conducted using a two-photon 8 kHz resonant scanner (Bruker) with a piezoelectric crystal was coupled to the objective as described previously[18] or an AOD microscope (ATLAS, Femtonics Ltd) as described previously[16]. The objective was a Nikon 16x x NIR water immersion, 0.8 NA, 3.0 mm working distance. The excitation laser was 920 nm (50-100 mW, Coherent). For some structural images in red, the laser was tuned to 960nm or performed with a 1070 nm fiber laser (Fidelity). Red (tdTomato or mRuby3) and green (GCaMP7f) channels were separated by emission cubes. Images were acquired at 1x, 1.5x, or 2x digital zoom, with 512 x 512 pixels. For multiplane imaging, the piezo was programmed to sequentially settle at 5 to 6 Z-depths, separated by 25 to 35 µm, and to wait at each plane for 15ms before acquiring the image. This wait time was necessary to avoid motion artifacts due to the vibrations involved with the fast plane jumps. When the piezo reverses direction, distance travelled between the last plane and the first plane (nearly 200µm) was however too high to acquire a stable image, and thus the first plane was always discarded for analysis. Ultimately, all settings were adjusted to keep the frame rate above 5 Hz.

Optogenetics and place field induction:

All optogenetic experiments were performed on Bruker microscopes. A dichroic mirror was used to allow red light to pass through into the brain, and green light to be reflected into the PMT. The stimulation was performed with an ultrafast and high-power collimated LED, at 625 nm (Prizmatix, 625 nm). It was triggered using an Arduino that gated the inverse photostimulation signal of the Pockels cell, which turns off briefly between mirror turnaround, as well as when the piezo reverses direction. The average power of the LED was 35-70 mW measured under the objective. This approach allowed us to protect our PMTs from the high-intensity illumination but still take the advantage of the fast, full-frame resonant galvo scanning without losing any frames during photostimulation.

For place field induction, a pulse of light of 1-1.5sec duration was delivered at a location randomly chosen on the belt for 4-6 laps, in order to recapitulate the procedure used in previous *in vivo* patch experiments[17,21] The location of the stimulation was moved to another random location on different PRE-POST imaging sessions.

Behavioral training:

After recovery from surgery, mice were handled for several days and habituated to head-fixation. Mice were subsequently water-restricted to 85-90% of their original weight and trained to run on a single-fabric, cue-free belt. Mice were trained to lick and receive water rewards (water was delivered in response to tongue contact with a capacitive sensor) at random locations along the belt. As performance improved, the number of rewards delivered on each lap decreased. After several days of training on this cue-free belt, the mice were trained on a 2m-long, cue-rich belt for randomly delivered water rewards. The belt consisted of three joined fabric ribbons and included some combination of the following tactile cues: colored pom poms, velcro, glue gun spikes, pink foam strips, and silver glitter masking tape.

Data acquisition and preprocessing:

Imaging was started after mice could run approximately 10 laps in 10 minutes (usually after 7-10 days of total training). The animals were imaged for 10-15min, twice per day separated by a 1-hour interval, and for 1 to 3 days, depending on brain stability and behavioral performance. All analysis codes were written in Python 2.7. Preprocessing steps such as motion correction and region of interests (ROIs) segmentation were performed as described previously[16,18] using the SIMA package[30] (1.3.2). Fluorescence was extracted from each ROI using the FISSA[31] package (0.6.1) to correct for neuropil contamination, using 8 patches of 50% the area of the ROI, and $\alpha = 0.1$ for sparseness regularizer. For each interneuron's resulting raw fluorescence trace, a baseline F was calculated by taking the 1st percentile in a rolling window of 30 s and a $\Delta F/F$ trace was calculated as previously described[16]. Relative fluorescence changes in CA1 PCs ($\Delta F/F$) were computed with a baseline calculation method adapted from previous studies[18], with uniform smoothing window t1 = 3 s and baseline size t2 = 60 s. For CA1 PCs, we then detected statistically significant calcium transients as described previously[18].

Spatial tuning curves:
For pyramidal cells, we used a previously described method[18]. Briefly, calcium transient onsets during running bouts of at least 1 s in duration were used to calculate the spatial information of the cell. Transients were randomly shuffled to different times during the running events, and the spatial information was recalculated. One thousand iterations were performed to create a null distribution for spatial information, and the cell was considered to be a place cell if its spatial information was above the 95th percentile of the null distribution. The belt was evenly divided into 100 spatial bins, and the place field was calculated from its transient rate map over these bins. The rate map was the number of transients in a given spatial bin normalized by the animal's occupancy in that spatial bin, which was then smoothed with a Gaussian kernel (s = 3 spatial bins). To detect individual place fields, each local maximum of the smoothed rate map was fitted with a Gaussian curve centered at that location. For each smoothed rate map, the place fields where the associated Gaussian was smaller than 50% of the largest Gaussian (by measuring the total area under the curve) were discarded. The remaining Gaussians were considered place fields.

For interneurons, the calcium fluorescence trace was used to approximate the firing activity over time, as previously described[16]. To calculate a spatial tuning curve for each interneuron, the treadmill was divided into 100 bins. For each bin, we calculated the average $\Delta F/F$ from frames where the animal was in locomotion (velocity > 5cm/s) and smoothed the resulting trace with a Gaussian kernel ($\sigma = 3$ bins) to obtain the spatial tuning curve

Determination of starter cell's spatial selectivity:
19 animals were used for the analysis of the relationship between the activity of a starter pyramidal cell and its presynaptic interneurons. Mice were imaged during 2 or 3 sessions and the data was separated based on the spatial selectivity of the starter neuron, reported in **Supplementary Table 2**. In the case where the spatial selectivity was identical on multiple sessions (which occurred only when the neuron was inactive), the first recorded session was used for analysis. The analysis of the development of negative tuning was performed for the mice in which spontaneous field formation was recorded and followed by a session where the field was stable from the first lap and active at the same location. In some animals, a stable field in the starter neuron was observed at a given location,

but then disappeared in the following session and ultimately a new field formed at the different location. In this case, the mice were not included for this analysis.

In-field selectivity (IFS) index:

Negative selectivity in interneurons was assessed by the in-field selectivity (IFS) index, defined as the difference over the sum of the average activity inside the field of the single CA1 PC and outside. Negative values indicate that the activity is higher outside the place field than inside, and positive values indicate higher activity within the place field. This index better represented the raw data than correlation of the interneurons and starter' tuning curves, because interneuron activity can have wider or smaller through activity than the starter's place field (see **Fig. 2a**). The same IFS window of 30cm centered around the peak of the place field and which corresponds to the mean place field width of all cells, was kept throughout all analyses in both the rabies tracing and optogenetics induction datasets.

Identification of recruited CA1 pyramidal cells

To determine which CA1 neuron was recruited by the photostimulation of the starter cell during place field induction, we used three distinct criteria. First, we defined the time during which photostimulation increased the density of calcium transients in the pyramidal cells above chance level. For a given brain, we repeated the place field induction protocol in the absence of a starter neuron (before electroporation) to estimate the baseline of transient density around photostimulation onset times. Then, we tested for each time point (in bins of 0.25s) the difference of transient proportion with and without a starter neuron. The first criterion for a recruited neuron was to have a transient in the statistically significant time window when transient density is higher than chance. The second criterion was based on the activity of the recruited neurons. To be identified, the average activity during laps of photostimulation needed to be higher than the average activity in laps preceding induction, for the location where the starters were induced. Third, to make sure that our identification did not pick already spatially selective recruited cells at that given location, any recruited neuron that matched the first two criteria but had a significant place field at the induced location was excluded for the analyses.

Probability of co-activity during immobility

To look at the time lag between neuron co-firing, we first generated a binarized trace for each neuron where all the frames were assigned the value 0, or 1 at the detected calcium onsets. For each neuron pair, we then calculated the cross-correlation by jittering the binarized traces between -2 and 2 seconds with one another. The co-activity probability was then taken as the sum of all the cross-correlograms divided by the number of pairs in total.

Network modelling:

Model architecture

Activity of neurons in the network is simulated by the following dynamic equations:

$$\tau\, dr_E/dt \;=\; -r_E + \Phi(W_{EE}\, r_E + \; W_{EI}\, r_I \;+\; \boldsymbol{s}_E) \qquad [1]$$
$$\tau\, dr_I/dt \;=\; -r_E + \Phi(W_{IE}\, r_E + \; W_{II}\, r_I \;+\; \boldsymbol{s}_I)$$

where r_E and r_I are the vectors of firing rates of N_E excitatory (E) and N_I inhibitory (I) neurons, respectively, and W is the matrix of connection weights, including connections between E to E (W_{EE}), E to I (W_{IE}), I to E (W_{EI}), and I to I (W_{II}) neurons. τ is the effective time constant of the network integration, and $\Phi(.)$ denotes the activation function of the network which we assume to be a linear rectified function: $\Phi(I) = 0\; for\; I < 0$; $\Phi(I) = I, for\; I >= 0$.

615 The external input to E and I neurons are represented by s_E and s_I. The input to neuron i is described
616 by, $s_i = w_i^f\,(s_i^b + s_i^m)$, where w_i^f is the feedforward weight (drawn from a uniform distribution
617 between $[0.5,1]$ for E and $[0.2,0.3]$ for I neurons). $s_i^b = 1 + \zeta$ is the baseline input independent of the
618 location of the animal (with ζ drawn from a uniform distribution between [-0.5,0.5]), and s_i^m denotes
619 the modulation of input based on the location:
620
621 $$s_i^m = m_i\ exp\,(\gamma\, cos\,[2\pi\,(x(t) - x_i^*)/L\,])\ /\ exp\,(\gamma) \qquad [2]$$
622
623 Here, $x(t)$ is the position of the animal at time t, and $x^*{}_i$ is the preferred spatial position of neuron i.
624 The position of the animal is obtained as $x(t) = V\,t$, where V is the velocity. $L = 2m$ is the total
625 length of the circular belt, and we assume that the animal runs at a constant velocity, $V = 2\ m/min$.
626 The preferred position of neurons $x^*{}_i$ is uniformly spread between $[0, L)$, for both E and I neurons.
627 The degree of spatial modulation of the response is determined by the modulation factor m (drawn
628 from a uniform distribution between $[0,1]$ for E and $[0,0.1]$ for I neurons), and the sharpness of the
629 spatial response profile is given by the exponent $\gamma = 10$.
630 Neurons are connected together with random connectivity. Connection from neuron j to neurons i,
631 c_{ij}, is drawn from a binomial distribution with probability ϵ ($c_{ij} = 1$, i.e. there is a connection, with
632 probability ϵ; $c_{ij} = 0$, i.e. there is no connection, with probability $1 - \epsilon$). E-E pairs are connected
633 sparsely, with a connection probability of 10% ($\epsilon_{EE} = 0.1$). Other connection types are more densely
634 established, with a connection probability of 50% ($\epsilon_{EI} = \epsilon_{IE} = \epsilon_{II} = 0.5$). On top of the random
635 connectivity, the starter cell (the k-th neuron, with k chosen randomly from $[1, N_E]$) in which the place
636 field is induced (either spontaneously or by optical induction) is assumed to be part of a subnetwork.
637 It comprises N_s E and I neurons (with neuron ids: $[k - N_s/2, k + N_s/2)$). The E-E and E-I (E→I and
638 I→E) connectivity between these neurons are elevated to 100% ($\epsilon_s = 1$). Self-connections are not
639 allowed throughout. If there is a connection from neuron j to neuron i ($c_{ij} = 1$), the weight of their
640 connection, w_{ij}, is in turn drawn from a uniform distribution between $[0, J]$, for E→{E,I}, and $[-J, 0]$, for
641 I→{E,I} synapses. $J = 0.075$.
642 We first stimulate the activity of the network before induction from Eq. 1. We refer to the activity of
643 neurons obtained in this stage as r_B. The starter cell is forced to be untuned at this stage by allowing
644 $m_k = 0$. Then, an extra input, s_I, is injected into the starter cell:
645
646 $$s_I = exp\,(\gamma\, cos\,[2\pi\,(x(t) - x_k^*)/L\,]\ /exp\,(\gamma) \qquad [3]$$
647
648 during the induction. We refer to the activity of neurons as a result of induction as r_I. Successful
649 induction is modelled by the establishment of this tuned input in subsequent stages. The changes in
650 the activity of neurons resulting from induction, $\delta r = r_I - r_B$, governs the plasticity in the network,
651 which is modelled in two stages. First, connections between the starter cell and the rest of E neurons
652 undergo synaptic potentiation according to the following rule:
653
654 $$\varDelta w_{jk}{}^p = <\delta r_k\ \delta r_j> \qquad [4]$$
655
656 where $<.>$ denotes the temporal average. The weights are updated according to: $w_{jk} \leftarrow w_{jk} +$
657 $\eta_p\,\varDelta w_{jk}{}^p$, for the existing synaptic connections ($c_{jk} = 1$), with η_p denoting the rate of synaptic

658 potentiation. The activity of the network with the updated weight (simulated according to Eq. 1), r_P,
659 then guides the next stage of plasticity which is governed by depression of E→I synapses according
660 to:
661

$$\Delta w_{ij}{}^{d} = -< \delta r_i \, \delta r_j > \qquad [5]$$

663

664 where j counts over E and i over I neurons. δr describes the change in activity after potentiation
665 stage relative to the baseline firing rates: $\delta r = r_P - r_B$. We update the network weights according to:
666 $w_{ij} \leftarrow w_{ij} + \eta_d \, \Delta w_{ij}{}^{d}$, for the existing synaptic connections ($c_{ij} = 1$), with η_d denoting the rate of
667 synaptic depression. If the weight of an E→I connection becomes negative after an update, it is set to
668 zero. $\eta_p = 100$ and $\eta_d = 5$.
669 The activity of the network is simulated (Eq. 1) with the final updated weights (Eqs. 4,5) to obtain the
670 final responses. Network activity is simulated before, during and after induction for $N_L = 10$ laps (each
671 lap lasting for $T_L = L/V = 60\,sec$), and the weights are updated based on the average activity across
672 all laps. We simulated the activity of 40 different starter cells and their presynaptic inhibitory networks
673 to obtain the results in **Fig. 2**. To expedite simulations, some experiments are performed with an
674 increased velocity of$V_s = 20\, m/min$; we check that this does not change the results. Default
675 parameters of the simulations are described in **Supplementary Table 4**.
676

677 *Anti-tuning in presynaptic interneurons argues for specific connectivity.*
678 Our experimental results showed that negative tuning emerged specifically in the presynaptic pool of
679 interneurons, and was absent in randomly sampled inhibitory populations. In the absence of
680 subnetworks, with no specific connectivity between E and I neurons, the starter cell would be
681 randomly connected to its presynaptic pool of interneurons. If any bias existed in the presynaptic pool
682 of the starter cell, it would also be present in randomly chosen pools of interneurons, and hence it
683 cannot be selective to presynaptic interneurons. Note that, even if the starter cell induces an anti-
684 tuning specifically in its postsynaptic pool of interneurons, this bias would not be reflected in its
685 respective presynaptic pool of interneurons, unless pre-/post-synaptic interneurons form a
686 reciprocally connected subnetwork with the starter cell. This reasoning was verified in our simulations,
687 where network models with only random connectivity did not show an emergence of anti-tuning
688 selective to presynaptic interneurons. The generation of inverse selectivity in the presynaptic partners
689 *in silico* can alternatively be achieved by specific connectivity in disinhibitory circuits. In this scenario,
690 place field formation in the starter cell can elevate the activity of interneuron-specific interneurons
691 (INT1) with specific contacts to the presynaptic ensemble (INT2) (**ED10**). We implemented one such
692 model and found that plasticity of E-to-I synapses can potentiate the disinhibitory motif (PC-to-INT1-
693 to-INT2-to-PC), leading to the emergence of negative selectivity in a presynaptic pool of interneurons
694 (INT2). However, in this configuration, INT2s that developed inverse selectivity were suppressed from
695 the beginning at the preferred location of the starter PC (**ED10**), which would not be consistent with
696 our previous results (**Fig. 3g**). Moreover, INT1s received stronger inputs from the starter PC as a
697 result of PC-to-INT1 potentiation and thus developed a strong positive tuning (**ED10**). We would
698 therefore expect to observe a significant increase in the activity of a subpopulation of IN1s
699 responsible for disinhibition. We tested this hypothesis by performing place field induction in VIP-Cre
700 animals, known to genetically label interneurons specializing in disinhibitory control of pyramidal cells.
701 In this set of experiments, we did not find significant differences between successful (+) and failed (-)

induction sessions, nor did we observe that VIP neurons increased their selectivity at the induced location (**ED10**), ruling out their potential involvement in the circuit mechanisms generating anti-selectivity.

Anti-tuning in presynaptic interneurons argues for collective dynamics.

Our network simulations also revealed that anti-selectivity in presynaptic interneurons do not emerge in network structures without specific E-E connectivity. This suggests that collective interaction of PC-PC subnetworks is involved in the generation of anti-tuning, and that single cell interactions may not provide an explanation for the emergence of anti-selectivity. To understand this better, we developed a model with only a single starter PC (**ED8**), which represents the extreme case of single-cell interaction with interneurons. Numerical simulation of such a model revealed that anti-tuning cannot emerge as a result of depressive mechanisms in a structure with specific connectivity of a single-cell and interneurons. Stronger depression of E-I synapses only diminished the tuning of presynaptic interneurons at the induced location, but did not lead to a negative tuning. Intuitively, this can be understood in terms of the reorganizations of weights between the starter PC and interneurons. Following induction of the place field in the starter PC, a depressive mechanism can decrease the weight of E→I synapses to interneurons with similar selectivity (denoted by red in **ED8a**). However, no matter how weak, the connection will still confer a net positive change in tuning towards the induced location at the postsynaptic interneuron, under the assumption that the starter PC was not tuned before the induction. On the other hand, (relative) potentiation of weights between the starter PC and interneurons tuned to other locations (denoted by blue in **ED8a**) would only increase the in-field selectivity of interneurons, on average. Thus, anti-Hebbian plasticity mechanisms are not able to generate anti-selectivity in interneurons if only applied at the single-cell level.

This reasoning can be presented more formally by the following mathematical argument. Suppose that an untuned cell with a baseline activity of r_0 at all locations changes its response and becomes selective to location x^*:

$$r \ = r_0(1 + cos\ (2\pi\ (x - x^*)/L)$$

The activity of the postsynaptic interneurons before induction is given by wr_0, where w is the weight of E→I connection before induction. After induction, the activity of postsynaptic interneurons changes to $\alpha w\ r_0(1 + cos\ (2\pi\ (x - x^*)/L)$, where αw is the weight after induction, with $\alpha > 1$ and $\alpha < 1$ describing synaptic potentiation and depression of E→I connections, respectively. The change in the activity of postsynaptic interneurons can therefore be written as:

$$\delta r_I \ = \alpha w\ r_0(1 + cos\ (2\pi\ (x - x^*)/L)\ - w\ r_0$$

The untuned component of the change in the activity of inhibitory neurons can be written as:

$$< \delta r_I >= (\alpha - 1)\ w\ r_0$$

where $<.>$ denotes the average across space. The tuned component of the change (spatial modulation, denoted by $<<.>>$) can, in turn, be described as:

$$<< \delta r_I >> = \alpha w\ \ cos\ (2\pi\ (x - x^*)/L)\ .$$

For $\alpha > 1$(synaptic potentiation) both the untuned and tuned components increase.

For $\alpha < 1$(synaptic depression), the untuned component becomes negative:

$$< \delta r_I >= (\alpha - 1)\ w\ r_0 < 0;\ for\ \alpha < 1$$

However, the tuned component would only become weaker, but still remain positive, as a result of synaptic depression:

$$<< \delta r_I >> = \alpha w\ \ cos\ (2\pi\ (x - x^*)/L)\ > 0;\ for\ \alpha < 1.$$

742 Therefore, in this setup, it is not possible to obtain negative tuning as a result of synaptic depression
743 of connections between a single PC and its post-/presynaptic interneurons.
744
745 *Limitations of the model*
746 Our model has some limitations. First, our model does not account for the initial bias in the
747 presynaptic pool of interneurons. Our experiments revealed a weak anti-tuning bias, prior to
748 induction, in the presynaptic inhibition of the pyramidal cells which successfully formed a place field.
749 In fact, in our model we saw the opposite bias: in the E-I subnetwork, there was a positive bias
750 towards the same place field, as I neurons receive input from E neurons with similar selectivity. In our
751 modelling, we assumed that synaptic plasticity changes connection weights as a result of response
752 changes after induction. It is, however, possible that similar plasticity mechanisms would be at play
753 even before induction, in the "baseline" state of the network. It would be interesting to see if similar
754 mechanisms can also explain the weak initial bias in the network, which in turn can guide the process
755 of induction towards starter cells belonging to the subnetwork, and hence explaining why induction
756 succeeds in some cells and why it fails in others. Secondly, the plasticity mechanisms in our model
757 are prone to instability. Potentiation of E-E synapses can lead to unstable modes of activity in the
758 network, if it is not controlled beyond a certain point. Depression of E-I weights, too, deprives the
759 network of potent recruitment of inhibition, which is necessary for its stability, especially following the
760 initial excitatory potentiation. It would be interesting to see which mechanisms provide such stability in
761 hippocampal networks of CA1. One possibility is homeostasis mechanisms, which control the firing
762 rate of neurons, but other mechanisms like E-I potentiation may also contribute to this. It would be
763 interesting to see if different subtypes of interneurons follow different patterns of plasticity and hence
764 contribute differently to this process.
765
766 *Calculation of transsynaptic labelling efficacy in local CA1 pyramidal cells:*
767 Anatomical studies[32] have provided a quantitative estimate that CA1 PCs make about 200 synapses
768 on local CA1 PC targets. Historically, these connections have been practically ignored in the field
769 because this estimated connection probability (200 out of about 150,000 CA1 pyramidal cells
770 ipsilaterally: ~0.13%) is lower than the ~1% collaterals in CA3[22]. However, we can calculate based on
771 our data that the local PC-PC contacts may be higher than 200. To do so, we can use the
772 transsynaptic efficacy at the CA3-CA1 synapses of ~0.5% derived from ~130 CA3 cells labeled
773 divided by 28,000±8,200 known CA3 synapses on CA1PCs[32]. Assuming the same RABV labeling
774 efficacy for the putative local PC contacts in CA1, we thus estimate that at most 1-3 presynaptic
775 CA1PCs (i.e., ~0.5% of the previously estimated 200 presynaptic CA1PCs targeting the starter
776 postsynaptic cell) would be expected to be labeled. Given our anatomical data, we find on average 11
777 presynaptic CA1 PCs labeled by the RABV. If we use the same efficacy as the CA3-CA1 synapses,
778 this would imply an order of magnitude more connections (~2000 PCs converging to 1 starter PC).
779 Alternatively, it is possible that the labeling efficacy for local CA1 PCs contacts is higher compared to
780 the more distant CA3 presynaptic cells.
781
782 **Statistics and reproducibility**:
783 All statistical tests are two-sided. No adjustments were made for multiple comparisons except for
784 ANOVAs with difference among groups deemed statistically significant (P>0.05). In these case,
785 Tukey's test was used post hoc and P-values were adjusted for multiple comparisons and always

786 indicated in the legends where appropriate. For comparisons between two populations, t-tests were
787 applied if the data points followed a normal distribution (confirmed using the Kolmogorov-Smirnov
788 test). To analyze data that were not normally distributed, the non-parametric Wilcoxon rank-sum test
789 (for unpaired samples) and Wilcoxon signed-rank test (for paired samples) were used.
790
791 Boxplots always represent median and interquartile range (IQR, 25th to 75th percentile) while whiskers
792 extend to cover the distribution without outliers (defined as points above 1.5 IQR below or above the
793 box edges). Bar plots always represent mean and s.e.m unless specified otherwise.
794
795 Representative *in vivo* images as well as histological experiments were repeated independently in
796 different mice with similar results for Figs. 1b, 1d ($n = 6$), 1i ($n = 19$), 3c ($n = 6$), 4a ($n = 13$) and
797 Extended Data Figs. 1a-g ($n = 6$), 1l ($n = 4$), 6a ($n = 13$), 10e ($n = 4$)
798

799 **Acknowledgements:**
800 A.L. is supported by the National Institute of Mental Health (NIMH) 1R01MH124047 and
801 1R01MH124867; the National Institute of Neurological Disorders and Stroke (NINDS)
802 1U19NS104590 and 1U01NS115530, and the Kavli Foundation. B.V. is supported by (NIH)
803 T32GN007367 and (NIMH) F30MH125628. A.J.M is supported by the Gatsby Charitable Foundation
804 (GAT3361) and Wellcome Trust (090843/F/09/Z). S.V.R. is supported by (NIMH) F31MH117892. F.P
805 is supported by (NINDS) R01NS067557 and R21NS109753-442 01A1. H.B is supported by (NINDS)
806 K99NS115984-01. We would like to thank Zuckerman Institute's Cellular Imaging platform for
807 instrument use and technical advice. Imaging was performed with support from the Zuckerman
808 Institute's Cellular Imaging platform, and the National Institute of Health (NIH 1S10OD023587-01).
809 We thank Dr. Steve Siegelbaum and members of the Losonczy lab for invaluable comments on the
810 manuscript.

811 **Author contributions:**
812 T.G. and A.L. conceived the study and wrote the manuscript. T.G performed all the experiments and
813 analyzed the data. T.G and B.V performed immunohistochemistry and tissue clearing. T.G, S.V.R and
814 A.N. developed the optogenetics induction and electroporation protocols. B.R. supported AOD
815 imaging-related software development. H.B, A.J.M. and F.P. produced viral and plasmid reagents.
816 S.S. and C.C. developed and implemented the computational model with inputs from T.G.
817

818 **Competing interests:**
819 The authors declare no competing interests.
820

821 **Data Availability Statement:**
822 All data are available from the corresponding authors upon reasonable request. Source data are
823 provided with this paper.
824

825 **Code availability**
826 All custom codes are available from the corresponding authors upon reasonable request.
827

828 **Extended Data Figure 1. Anatomical location of presynaptic neurons targeting a single CA1**
829 **pyramidal cell (Supplementary Table 1).**
830 **a,** Representative coronal slice of the dorsal CA1 hippocampus with the starter pyramidal cell
831 expressing the fluorophore Venus (green), TVA receptor and glycoprotein G, after electroporation. **b,**
832 Coronal slice of the hippocampus 14 days after rabies injection. Neurons in red expressing tdTomato
833 are presynaptic to the starter cell. **c-e,** Presynaptic neurons can be found in the entorhinal cortex,
834 medial septum and supramammillary nucleus (**a** to **d**, blue is DAPI) **f,** In vivo two-photon images of a
835 starter neuron (green) and presynaptic neurons (red). **g,** Post hoc immunohistochemistry labeling of
836 the same tissue reveals that the HA tag fused with the TVA receptor is uniquely expressed in the
837 starter neuron, indicating that rabies tracing is restricted to this individual cell. Scale bars are 50µm.
838 **h,** Lateral distribution of the presynaptic interneurons (red) and unlabeled interneurons (gray)
839 calculated on in vivo two-photon Z-stacks (n = 7 mice). Coordinates (0, 0) indicate the location of the
840 starter neuron. **i,** Same, but for depth distributions. *S.O: stratum oriens, S.P: stratum pyramidale, S.R:*
841 *stratum radiatum.* **j,** Strategy to generate VGAT-EYFP mice in which EYFP is expressed in all
842 inhibitory interneurons. **k,** Schematic of the experiment. A starter cell is electroporated in a VGAT-
843 EYFP animal, followed by injection of a RABV-tdTomato. As a result, presynaptic interneurons will co-
844 express EYFP and tdTomato and presynaptic pyramidal cells will express only tdTomato. **l,**
845 Representative confocal images of the starter cell (left), presynaptic and unlabeled interneurons
846 (middle) and presynaptic pyramidal cells (right). Scale bars are 50µm**. m,** Quantification for 4 animals
847 across the ipsilateral CA1.
848
849 **Extended Data Figure 2. Spontaneous place field formation is not associated with detectable**
850 **decrease in the level of presynaptic inhibition (Supplementary Table 2).**
851 **a**, Representative trace of the starter neuron's fluorescence activity during navigation. The first
852 transient (pink) corresponds to the spontaneous formation of a place field, as shown in the
853 fluorescence heatmap (bottom). Fluorescence amplitude of the calcium transient during field
854 formation is significantly higher than all other subsequent events (n=11 mice, paired t-test, P=0.008).
855 **b,** Lap-average (n=11 networks) activity (mean±s.e.m.) of the presynaptic (red) and unlabeled (gray)
856 interneurons centered around the onset lap of field formation (starter, blue) from. **c,** Inhibition levels in
857 both populations remained relatively constant before and after formation. All groups n=11, One-way
858 ANOVAs: starter, P=0.0004 (post hoc Tukey's tests with P-values adjusted for multiple comparisons:
859 all P<0.05); presynaptic: P=0.32; unlabeled P=0.68 **d,** Average tuning curve (mean±s.e.m, all n = 11
860 networks) centered around the starter's place field for the presynaptic and unlabeled interneurons at
861 three different time points during field formation, showing no immediate spatial reconfiguration of their
862 responses. **e,** Same analysis using population-vector correlation before and at lap formation onset for
863 the presynaptic interneurons. **f,** Distribution of in-field selectivity index (IFS) for presynaptic
864 interneurons before and during the lap of field formation, showing no change in spatial selectivity at
865 the field's location (n=199 from 11 mice). **g,** Distribution of the IFS difference (n=199 from 11 mice)
866 compared to a shuffle distribution where the location of the starter's place field is randomized on the
867 belt.
868
869 **Extended Data Figure 3. Presynaptic interneuron spatial responses are not spatially selective**
870 **when the starter is inactive and do not immediately reconfigure after spontaneous field**
871 **formation (Supplementary Table 2).**

872 **a,** Normalized average tuning curves of the starter neurons (blue), their presynaptic partners (red)
873 and unlabeled interneurons (gray), centered around the middle of treadmill. Thick line represents the
874 average for n = 14 mice and shaded area the s.e.m. **b,** Boxplots of IFS values for all 14 mice,
875 averaged at the network level (paired t-test, P = 0.32). **c,** In-field selectivity (IFS) index for all
876 presynaptic (n = 223) and unlabeled (n = 1730) interneurons from n = 14 mice, P = 0.19
877 (Kolmogorov-Smirnov two sample test). Negative IFS indicates negative selectivity in the starter's
878 place field. Insets (mean ± s.e.m), P = 0.42 (t-test). **d,** IFS values were computed in ***b*** and ***c*** for a
879 virtual place field in the middle of the treadmill. Here, each point represents the t-test's P-values for
880 IFS values of presynaptic vs. unlabeled interneurons while iteratively moving the location of the virtual
881 field along the belt and recomputing the IFS at each location. This analysis shows that there is no
882 difference in spatial selectivity anywhere on the belt when the starter cell has no place field. **e,**
883 Experimental timeline: mice were imaged twice a day. Between each imaging session, they were
884 allowed to rest in their home cage for one hour (also see Methods). In n = 4 mice, we tracked the
885 spontaneous emergence of a place field in the starter neuron and its persistence in a later session. **f,**
886 Representative heatmap activity for a starter cell as a function of lap (y-axis) and position (x-axis) on
887 the belt. Field creation occurred in the first session of the day at lap 4 (white arrow) and persisted
888 after rest in a later session at the same location. **g,** Session-average tuning curve for the starter cell
889 shown in **f** and 6 of its presynaptic interneurons, reconfiguring their response and developing anti-
890 selectivity around the starter's place field (dashed line) in the later session. **h,** Cell-by-cell correlation
891 coefficients between the spatial response in the first session when the field emerged (creation) and a
892 later session (stable) for the presynaptic (n=81) and unlabeled (n=267) neurons from 4 mice, P = 0.04
893 (unpaired t-test). **i,** Same analysis but for network averages (n = 4 mice), P = 0.26 (Paired t-test pre.
894 vs unlab). **j,** Difference between the presynaptic and unlabeled interneurons average activity centered
895 around the starter's place field (gray), for both creation (top) and stable field session (bottom). In
896 purple, P-values between the two distributions as a function of position on the belt. Purple shaded
897 area indicates positions where P<0.05. Notice the dip in activity in the stable session indicating the
898 development of anti-selectivity in the presynaptic ensemble when the starter cell has an already
899 established place field. All boxplots represent median (central line) and interquartile range (25th and
900 75th percentile) while whiskers extend to the most extreme data points (excluding outliers).
901

902 **Extended Data Figure 4. Photostimulation of a single pyramidal cell increases interneuron**
903 **activity**

904 **a,** *Left:* Peri-stimulus time histogram (mean ± s.e.m) centered around the onset of the LED
905 stimulations for all interneurons (green, n = 2613 from 6 mice) and a shuffle trace where LED onsets
906 were randomly shuffled in time in each session (gray, same n). *Right:* Quantification of increased
907 activity (data, $P < 10^{-10}$; shuffle, P = 0.12, one-sample t-tests). Data vs shuffle, $P<10^{-10}$ (paired t-test).
908 **b,** Same analysis as **a** but all traces are averaged (n = 14 sessions in 6 mice, mean ± s.e.m) for a
909 given session (data, P=0.002; shuffle, P=0.23, one-sample t-tests). Data vs shuffle, P=0.003 (paired
910 t-test). **c,** Difference in IFS between the PRE and POST session as a function of increased ΔF/F
911 during optogenetics stimulations ((+), n=1208, $P<10^{-7}$; (-), n=1157, P=0.12; Pearson's R, n = 6 mice).
912 **d,** Same as **c** but for the IFS in PRE only ((+), n=1208, P=0.00012; (-), n=1190, P=0.15; Pearson's R,
913 n = 6 mice). **e,** Mice velocity (mean ± s.e.m) centered around LED stimulations during place field
914 induction, separated by whether induction was successful (magenta, n = 15 sessions) or failed (gray,
915 n = 13 sessions) from 10 mice (VGAT-Cre and VIP-Cre). Notice that animals slightly slow down

916 during light presentation (1-1.5s stimulations) but continue running at relatively constant and high
917 speeds. **f,** Difference in speed before and after LED stimulations from **e** for each condition. (+),
918 P=0.53; (-), P=0.85 (one-sample t-tests). (+) vs (-), P=0.75 (t-test). **g,** Three-dimensional
919 representation of all recorded interneurons (n=1208 from 6 mice) for successful inductions (+) plotted
920 as a function of their distance in situ to the seed neuron (centered at x, y, z = 0, 0, 0). Both color code
921 and circle size indicate the change in IFS between PRE and POST sessions. **h,** Projection of **g** onto
922 the Z-axis (depth) shows no distance-dependent relationship (n=1208 from 6 mice, P=0.29,
923 Pearson's R). **i**, Projection of **g** onto the X-Y axes. **j,** Euclidean distance (X-Y) to the seed neuron as
924 a function of change in IFS shows significant relationship (n=1208 from 6 mice, P=0.012, Pearson's
925 R). Red bins represent the running IFS average value along the XY distance. All boxplots represent
926 median (central line) and interquartile range (25th and 75th percentile) while whiskers extend to the
927 most extreme data points (excluding outliers).
928
929 **Extended Data Figure 5. No immediate spatial reconfiguration of interneurons following place**
930 **field induction**
931 **a,** Average spatial tuning curve for all interneurons (n = 6 mice) for the laps before place field
932 induction (pre-stim laps), directly following induction (post-stim laps) and in POST following
933 successful (magenta) or failed (gray) inductions. Interneurons are ordered by their IFS, and centered
934 around the induced location for each condition. **b, I**FS values on a cell-by-cell basis, showing that
935 interneurons do not become immediately negatively selective at the induced location following
936 successful induction. *Top*, comparison of IFS in pre-stim laps vs. post-stim laps for successful (+) and
937 failed (-) inductions. (-), P = 0.81; (+), P = 0.06 (Wilcoxon signed rank-tests). (-) vs (+), P = 0.07
938 (Wilcoxon rank-sum test). *Bottom*, comparison between post-stim laps and POST session (1 hour
939 after rest). (-), P = 0.24; (+), $P < 10^{-10}$ (Wilcoxon signed rank-tests). (-) vs (+): $P < 10^{-10}$ (Wilcoxon
940 rank-sum test). For top and bottom, interneurons recorded in all three sessions: n = 1190 for (+) and
941 n = 1208 for (-) from 6 mice. **c,** 2D histogram of interneurons' IFS in pre-stim laps and POST session
942 (same *n* as **b**). (+), $P < 10^{-10}$; (-), $P < 10^{-10}$ (Pearson's R). **d,** Average IFS values at the session level
943 (n = 7 for each condition from 6 mice) before, immediately after and in the POST induction session. (-
944), all P > 0.05 (paired t-tests). (+), prestim vs POST, P = 0.04; all others P > 0.05 (paired t-tests). **e,**
945 Fraction across 6 mice of negatively selective interneurons (IFS < 0) before induction and in the
946 POST session. POST(+) vs prestim(+), P = 0.0003 ; POST(+) vs prestim(-), P = 0.0003 ; POST(+) vs
947 POST(-), $P<10^{-5}$ (Fisher's exact tests). **f,** Difference in fraction of negatively selective interneurons
948 (mean ± s.e.m) between prestim and POST for each session (n = 7 for each condition from 6 mice).
949 (+) vs (-), P = 0.028 (t-test). **g,** Overall fraction of negatively selective interneurons in prestim (top)
950 and POST (bottom) sessions for successful (magenta) and failed (gray) inductions across 6 mice
951 (same n as **e**), calculated as a function of position on the belt and not only at the location where the
952 seed neuron is induced (corresponding to position 0 here). All boxplots represent median (central
953 line) and interquartile range (25th and 75th percentile) while whiskers extend to the most extreme data
954 points (excluding outliers).
955
956 **Extended Data Figure 6. Photostimulation of a starter neuron entrains activity in other**
957 **surrounding pyramidal cells.**
958 **a,** Representative field of view with one starter pyramidal cell (red) electroporated with bReaChes and
959 GCaMP expressed in all PCs**.** Optogenetic stimulations (arrows) drive activity in the starter neuron

and evoke calcium events in other surrounding pyramidal cells. **b,** Quantification of increased fluorescence (post minus pre) for each photostimulation of the seed neuron (*left*, red, n = 31 sessions, $P<10^{-10}$, t-test) and all other pyramidal cells (*right*) in 13 mice. The presence of a seed neuron with an excitatory opsin recruits other PCs above chance level. With seed (blue), n = 31 sessions, $P<10^{-5}$; without seed (black), n = 8 sessions, P=0.59 (t-tests). With vs without seed, P= 0.013 (t-test). **c,** Intersomatic distance between recruited PCs and the starter neuron for successful (magenta, n =13 sessions) and failed inductions (gray, n = 18 session), P = 0.19 (t-test) from 13 mice. **d,** Number of recruited pyramidal cells for each condition, P = 0.36 (Wilcoxon rank-sum test), same *n* as **c**. **e,** Fraction of recruited pyramidal cells that were place cells in the PRE session before photoinduction, minus the rate of place cells detected in the other non-recruited cells, for each session, P = 0.28 (Wilcoxon rank-sum test), same *n* as **c**. **f,** Fraction of recruited pyramidal cells that are place cells in the POST session after photoinduction, minus the rate of place cells detected in the other non-recruited cells for each session, P = 0.005 (Wilcoxon rank-sum test), same *n* as **c**. **g,** During immobility and before the seed neuron was induced, the recruited neurons are more likely to spontaneously co-fire (see Methods) than what would be expected by chance – here calculated by selecting an equivalent number of random pairs of neurons (n = 2205 pairs from 13 mice with neurons with at least 1 transient, mean ± s.e.m). **h,** Similar to **g**, pairwise correlation of activity traces averaged for each session (n = 28 containing bouts of immobility before induction, from 13 mice) during immobility before seed induction. Recruited, P=0.0003; Shuffled, P=0.10 (t-tests). Recruited vs shuffled, P = 0.027 (t-test). **i,** This like-to-like relationship among recruited cells is more pronounced for neurons whose intersomatic distances (mean ± s.e.m) are within 150µm of one another (n=2402 pairs from 13 mice). Same assembly pairs, P=0.0008; Shuffled pairs, P=0.83 (t-tests). **j,** Pairwise distance (mean ± s.e.m) of place field centroids for recruited and shuffled neurons (n = 494 pairs from 13 mice) during navigation in laps preceding induction. Chance level is represented by a dashed line: Recruited, $P<10^{-5}$; Shuffled, P = 0.89 (t-tests). Recruited vs shuffled, $P<10^{-5}$ (t-test). **k,** Similar to **i**, this effect is more pronounced for closer neurons (mean ± s.e.m). Same assembly pairs, P=0.048; Shuffled pairs, P=0.40 (t-tests), same *n* as **j**. All boxplots represent median (central line) and interquartile range (25th and 75th percentile) while whiskers extend to the most extreme data points (excluding outliers).

Extended Data Figure 7. Place field induction in an individual neuron does not influence the global representation of the environment

a, Representative examples of five sessions (from 5 distinct mice) showing the location of the place field of recruited neurons that became place cells from PRE to POST, for each condition (POST+: successful induction in the seed neuron, POST-: failed induction). Position 0 represents the location where the seed neuron was induced in PRE. **b,** *Left*: Heatmaps representing the activity for all recruited cells as a function of position on the belt, centered around the induced location. Photoinduction (labeled ‘during stim’) drives a large increase in activity in the recruited cells, which was not present before induction (left, ‘before stim’). *Right*: distribution of the peaks of the spatial responses before (n = 243) and during (n = 306) photoinduction from 13 mice ($P<10^{-10}$, two-sample Kolmogorov-Smirnov test). During, $P<10^{-10}$; before, P = 0.19 (Kolmogorov-Smirnov uniformity tests). **c,** *Left*: Place field distribution of all the non-recruited place cells in the POST session for each condition. *Right*: Distribution of place field peaks from 13 mice (P = 0.13, two-sample Kolmogorov-Smirnov test). (+) (n = 1175), P = 0.67; (-) (n = 1177), P = 0.26 (Kolmogorov-Smirnov uniformity

004 tests). **d,** *Left:* Place field distribution of non-recruited cells which formed a field in the POST session
005 (not place cells in PRE but place cells in POST), for each condition from 13 mice. *Right*: Distribution
006 of place field peaks (P = 0.12, two-sample Kolmogorov-Smirnov test). (+) (n = 856), P = 0. 34; (-) (n =
007 904), P = 0. 10 (Kolmogorov-Smirnov uniformity tests).
008
009 **Extended Data Figure 8. Computational network model with single neurons and preferential**
010 **connectivity cannot explain inverse selectivity in presynaptic interneurons.**
011 **a,** Model with a single seed pyramidal cell. For all following analyses, the structure and parameters of
012 the network is similar to *Figure 4* with the same number of seed neurons (n = 40). Specifically, the
013 seed neuron has both random and specific connectivity with interneurons, with the same Ns (number
014 of units within the subnetwork). **b,** *Right:* average activity of interneurons from the subnetwork of the
015 starter cell (subnet.) and from the rest of the network (rand.). *Right*: in-field selectivity (IFS, mean ±
016 s.e.m) for interneurons presynaptic (n=2322) to the starter cell (presyn., n = 2322) and others (rand.,
017 n = 1696). **c,** Same as **b** (mean ± s.e.m), when there is no depression between the starter cell and
018 interneurons (d=0; n = 2301 presyn.; n = 1699 rand.). **d,** Same as **b** (mean ± s.e.m), for stronger
019 depression rate of synapses (d=50; n = 2283 presyn.; n = 1717 rand.). **e-h,** Simulation of the network
020 model with different sizes of the pyramidal cell-interneuron subnetwork (Ns). Other parameters are
021 the same as in *Extended Data Figure 9*, which is copied here in **f** for comparison. **e,** IFS values
022 (mean ± s.e.m) for 10 pyramidal cells and 10 interneurons (Ns = 10; n = 4436 presyn.; n = 3564
023 rand.). **f**, IFS values (mean ± s.e.m) for Ns = 15 (n = 4611 presyn.; n = 3389 rand.). **g,** IFS values
024 (mean ± s.e.m) for Ns = 20 (n = 4843 presyn.; n = 3157 rand.). **h**, IFS values (mean ± s.e.m) for Ns =
025 25 (n = 5064 presyn.; n = 2936 rand.). The results are robust to change of the parameter, especially
026 larger subnetworks lead to more prominent presence of the anti-tuning in presynaptic inhibition.
027 Smaller subnetworks make the detection of anti-tuning difficult, although the effect is still observable
028 in the average activity.
029
030 **Extended Data Figure 9. Computational model with subnetwork structure with different**
031 **connectivity motifs.**
032 **a,** Spatial tuning of all pyramidal cells (left) and interneurons (right) in the networks from 40
033 simulations (similar in the following **b-e**), sorted according to their in-field selectivity (IFS). Position is
034 expressed relative to the location of place formation in the starter cells, respectively. **b,** *Left*: Average
035 activity of interneurons within the subnetwork (subnet.) and from outside (rand.) as a function of
036 position. *Right*: IFS (mean ± s.e.m) for interneurons presynaptic to starter cells (presyn., n = 2335)
037 and others (rand., n = 1789). The results are shown for the full model (Figure 4) with pyramidal cell-
038 interneuron subnetwork structure (illustrated on the top). **c,** Same as **b** (mean ± s.e.m) for network
039 structures with random connectivity and without the specific connectivity structure of the starter-cell-
040 interneuron subnetwork (n = 1964 presyn.; n = 2043 rand.). **d,** Same as **b** (mean ± s.e.m) without the
041 specific connectivity of starter-PCs, while starter-interneurons preserve their specific connectivity (n =
042 2339 presyn.; n = 1669 rand.). **e,** Schematic illustration of the reorganization of activity and network
043 interactions following field formation. The starter cell elevates the activity of pyramidal cells and
044 interneurons within the subnetwork at its selective location (*left*), which is followed by depression of
045 pyramidal cells-to-interneurons connections, leading to the diminished activity of interneurons within
046 the subnetwork at that location (*right*).
047

Extended Data Figure 10. Alternative model with direct disinhibitory circuitry

a, *Top*: schematic of the circuit before field formation. A starter pyramidal cell (PC) contacts two interneuron entities (INT1 and INT2) with excitatory connections. INT1 (interneuron-selective interneuron such as VIP) exerts static inhibition onto INT2, which projects back to PC. *Bottom*: in this model, formation of a field in the starter PC drives INT1s and INT2s, but a stronger connectivity with INT1 leads to the depression of INT2 responses. **b,** Evolution of neuronal activity of the starter PC (left), INT1 (middle) and INT2 (right) following place field formation of the PC on lap 1. **c,** Average tuning curves before field formation (initial), during the formation (middle) and after field has formed (final), showing that INT2 ultimately exhibits negative tuning at that field location. **d,** Evolution of the synaptic weights as a function of time (laps) during the process of field formation. This model has experimentally testable predictions that we performed. **e,** To do so, we performed calcium imaging in VIP-Cre animals, known to genetically label a subset of interneuron-specific interneurons (INT1) and single-cell electroporation in an individual PC (seed) to perform place field induction. *Left*: schematic of the experiment. Right: In vivo two-photon image of GCaMP-expressing VIP interneurons (green) and a single CA1 PC expressing GCaMP and bReaChes (red). Scale bar is 50µm. **f,** PSTH (mean ± s.e.m) centered at the onset of the LED photostimulation for all VIP interneurons and a shuffle trace where LED onset was randomly chosen during the imaging session (n = 6 sessions in 4 mice). **g,** Boxplots representing the increased activity following LED stimulation. Data, P=0.18; Shuff., P=0.30 (t-tests). Data vs Shuff, P=0.8 (t-test). The lack of increased activity during photostimulation goes against the prediction of our model that field formation should elevate responses in the INT1 population. **h,** Distribution of in-field selectivity (IFS) at the induced location for all VIP interneurons before photoinduction (PRE, n = 774), and after successful (POST(+), magenta, n = 439) and failed (POST(-), gray, n = 353) inductions. Data from n = 14 sessions in 4 mice. All P > 0.05 (unpaired t-tests). The lack of development of positive selectivity is not consistent with our model (see **c**). **i,** Average spatial tuning curve for all interneurons for the laps before place field induction (PRE), and in the POST session following successful (magenta) or failed (gray) inductions. Interneurons are ordered by their IFS, and centered around the induced location for each condition. **j,** Boxplots representing IFS values for all VIP-positive interneurons (same n as **h**). PRE vs POST(-), P = 0.43; PRE vs POST(+), P = 0.37 (t-tests). All boxplots represent median (central line) and interquartile range (25th and 75th percentile) while whiskers extend to the most extreme data points (excluding outliers).

a 2p-guided electroporation in CA1
2p
glass pipette
cannula
skull
TVA800-HA
N2c(G)
Venus
Alexa488
CA1
CA3
DG
s.o
s.p
s.r

b electroporation
48-72h later
expression

c Rabies tracing
EnvA-N2cΔG-tdTomato
presynaptic neurons
14 days later

d Cleared tissue
CA1
CA2
CA3
D
P
M

e
Fraction presynaptic neurons
100
80
60
40
20
0
ipsi.
contra.
***
**
***
*
CA1
CA2
CA3

f Time (days)
0 injection
3 implant
10 electro-poration
20 imaging
22 rabies injection
36 tracing

g rAAV-(GCaMP7f)Cre
dCA1
7 days
VGAT-Cre

h TVA800-HA; N2c(G)
GCaMP7s; mRuby3
s.o
s.p
s.r
GCaMP-expressing interneurons

i Before RABV injection
GCaMP
mRuby3
After RABV injection
GCaMP
tdTomato

j Head-fixed spatial task
velocity
30 cm/s
20s
Fluorescence (ΔF/F)
presynaptic
unlabeled
200%

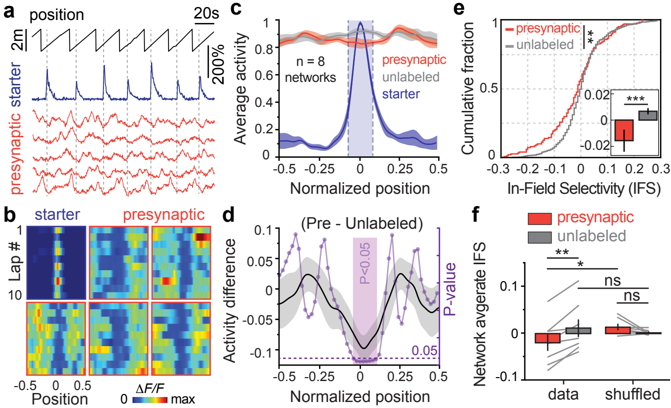
a
position
20s
2m
200%
starter
presynaptic
b
starter
presynaptic
Lap #
1
10
-0.5
0
0.5
Position
ΔF/F
0
max
c
Average activity
n = 8
networks
presynaptic
unlabeled
starter
Normalized position
d
(Pre - Unlabeled)
Activity difference
P<0.05
P-value
0.05
Normalized position
e
Cumulative fraction
presynaptic
unlabeled
**
***
In-Field Selectivity (IFS)
f
presynaptic
unlabeled
Network avgerate IFS
**
*
ns
ns
data
shuffled

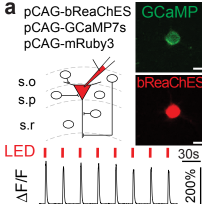
a
pCAG-bReaChES
pCAG-GCaMP7s
pCAG-mRuby3
GCaMP
bReaChES
s.o
s.p
s.r
LED
30s
ΔF/F
200%

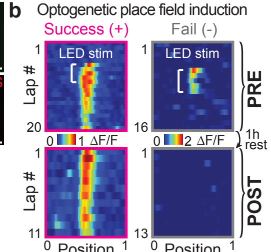
b
Optogenetic place field induction
Success (+)
Fail (-)
LED stim
LED stim
Lap #
PRE
1h rest
POST
0 1 ΔF/F
0 2 ΔF/F
Position

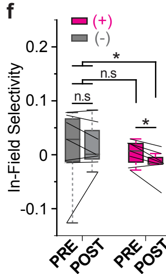
f
(+)
(-)
In-Field Selectivity
n.s
n.s
*
*
PRE
POST
PRE
POST

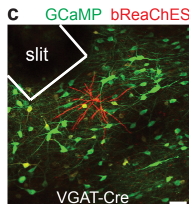
c
GCaMP bReaChES
slit
VGAT-Cre

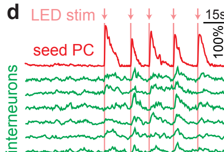
d
LED stim
15s
seed PC
100%
interneurons

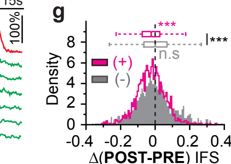
g
***
***
n.s
(+)
(-)
Density
Δ(POST-PRE) IFS

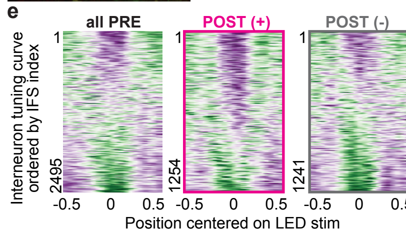
e
all PRE
POST (+)
POST (-)
Interneuron tuning curve ordered by IFS index
Z-score
1.5
-1.5
Position centered on LED stim

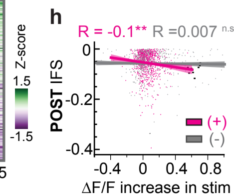
h
R = -0.1** R =0.007 n.s
POST IFS
(+)
(-)
ΔF/F increase in stim

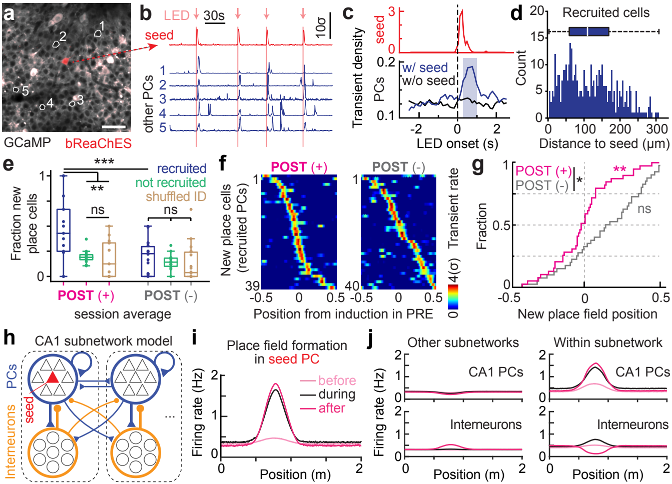
a
1
2
5
4
3
GCaMP
bReaChES
b
LED
30s
10σ
seed
other PCs
1
2
3
4
5
c
seed
3
0
Transient density
PCs
0.2
0.1
w/ seed
w/o seed
-2
0
2
LED onset (s)
d
Recruited cells
20
15
10
5
0
Count
0
100
200
300
Distance to seed (μm)
e
***
recruited
not recruited
shuffled ID
**
ns
ns
Fraction new place cells
1
0
POST (+)
POST (-)
session average
f
POST (+)
POST (-)
New place cells (recruited PCs)
1
39
1
40
-0.5
0
0.5
-0.5
0
0.5
Position from induction in PRE
Transient rate
4(σ)
0
g
1
POST (+)
POST (-)
*
**
ns
Fraction
0.5
0
-0.5
0
0.5
New place field position
h
CA1 subnetwork model
PCs
seed
Interneurons
...
i
Place field formation in seed PC
before
during
after
Firing rate (Hz)
2
1
0
0
Position (m)
2
j
Other subnetworks
Within subnetwork
CA1 PCs
CA1 PCs
Interneurons
Interneurons
Firing rate (Hz)
2
1
0
2
1
0
0
Position (m)
2
0
Position (m)
2